Structure Functions at High Q^2

Anthony T. Doyle*

* *University of Glasgow*[1]
Department of Physics and Astronomy, Glasgow, G12 8QQ

Abstract. Progress in the study of structure functions in deep inelastic scattering is reviewed. A brief introduction to the formalism and the status of global analyses of parton distributions and their uncertainties is given. The review focuses on recent developments in the following areas: HERA results on F_2, F_L and charm; the resolution of the CCFR-NMC discrepancy; Tevatron jet cross-sections at different energies; and HERA high-Q^2 cross-sections and the measurement of xF_3.

Introduction

The neutral current (NC) cross-section $l(k)N(p) \to l(k')X(p')$ for a lepton (e, μ) with four-momentum k scattering off a nucleon with four-momentum p can be expressed as

$$\frac{d^2\sigma(l^{\pm}N)}{dx\,dQ^2} = \frac{2\pi\alpha^2}{xQ^4} \cdot [Y_+F_2(x,Q^2) \mp Y_-xF_3(x,Q^2) - y^2F_L(x,Q^2)]$$

where Q^2 is the four-momentum transfer squared, $x = Q^2/2p \cdot q$ is the Bjorken scaling variable, $y = p \cdot q/p \cdot k$ is the inelasticity variable and $Y_{\pm} = 1 \pm (1-y)^2$. The contribution from F_2 dominates the cross-section and is measured directly. To investigate sensitivity to F_L at large y or xF_3 at large Q^2, the reduced cross-section

$$\tilde{\sigma} \equiv \frac{xQ^4}{2\pi\alpha^2}\frac{1}{Y_+}\frac{d^2\sigma}{dxdQ^2} \equiv F_2 \mp \frac{Y_-}{Y_+}xF_3 - \frac{y^2}{Y_+}F_L$$

is adopted. The contribution from F_L is a QCD correction which is important at large y: the characteristic y dependence is utilised in the determination of F_L at low Q^2. The contribution from xF_3, due to γZ interference and Z exchange, violates parity conservation and enters for $Q^2 \simeq M_Z^2$: the change of sign for opposite charges of the incoming lepton beam enable xF_3 to be extracted. In the quark parton model

[1] supported by PPARC and the Royal Society.

(or in the DIS scheme of NLO QCD) F_2/x is the "charge-weighted" sum of the quark densities

$$F_2(x,Q^2) = x\sum_f A_f(Q^2)\cdot\Sigma(x,Q^2)$$

where $A_f(Q^2) = e_f^2 - 2v_l v_f e_f P_Z + (v_l^2+a_l^2)(v_f^2+a_f^2)P_Z^2$ contains vector and axial terms due to γ, γZ interference and Z exchange respectively, $P_Z = 1/(4\sin^2\theta_W\cos^2\theta_W)\cdot Q^2/(Q^2+M_Z^2)$ is the Z propagator term and $\Sigma(x,Q^2) = q_f(x,Q^2)+\bar{q}_f(x,Q^2)$ is the singlet summed quark and anti-quark distributions. Similarly,

$$xF_3(x,Q^2) = x\sum_f B_f(Q^2)\cdot q_{NS}(x,Q^2)$$

where $B_f(Q^2) = 2a_l a_f e_f P_Z + 4v_l a_l v_f a_f P_Z^2$ contains vector and axial terms due to $\gamma - Z$ and Z exchange respectively, and $q_{NS}(x,Q^2) = q_f(x,Q^2) - \bar{q}_f(x,Q^2)$ is the non-singlet difference of the quark and anti-quark (valence quark) distributions.

The charged current (CC) cross-section $l^+(l^-)N \to \nu(\bar{\nu})X$ proceeds via W exchange and can be expressed as

$$\frac{d^2\sigma^{CC}(l^\pm N)}{dx\,dQ^2} = \frac{G_F^2}{4\pi x}\left(\frac{M_W^2}{Q^2+M_W^2}\right)^2$$

where G_F is the Fermi constant and a positive (negative) charged lepton beam picks out valence d (u) quarks.

Given a phenomenological input as a function of x, the parton distributions are evolved to different physical scales (Q^2) via the DGLAP evolution equations. The non-singlet contribution evolves as

$$\frac{\partial q_{NS}(x,Q^2)}{\partial t} = \frac{\alpha_s(Q^2)}{2\pi}P_{qq}^{NS}\otimes q_{NS}(x',Q^2)$$

where $t = \ln(Q^2/\Lambda^2)$ and the P_{ij}'s represent the NLO DGLAP splitting probabilities for radiating a parton with momentum fraction x from a parton with higher momentum x'. Quantities such as xF_3 provide a measure of $\alpha_s(Q^2)$ which is insensitive to the a priori unknown gluon distribution. Similarly, the singlet quark and gluon densities are coupled via the matrix equation

$$\frac{\partial}{\partial t}\begin{matrix}\Sigma(x,Q^2)\\ g(x,Q^2)\end{matrix} = \frac{\alpha_s(Q^2)}{2}\begin{matrix}P_{qq}\ P_{qg}\\ P_{gq}\ P_{gg}\end{matrix}\otimes\begin{matrix}\Sigma(x',Q^2)\\ g(x',Q^2)\end{matrix}$$

and quantities such as F_2 provide input for $\Sigma(x,Q^2)$ as well as coupled knowledge of $\alpha_s(Q^2)$ and the gluon, $g(x,Q^2)$. The gluon distribution, $g(x,Q^2)$, is determined through the scaling violations of F_2 at low x or constrained via jet or direct photon production at large x (where the gluon enters directly).

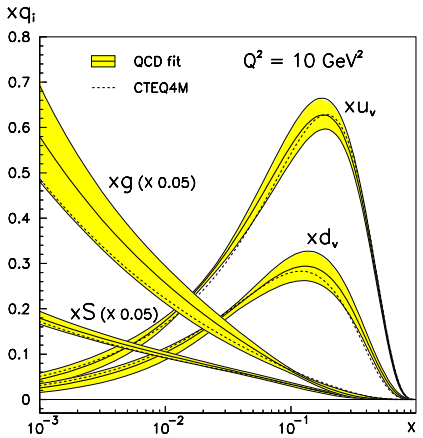

FIGURE 1. Parton momentum densities (full curves) at $Q^2 = 10\,\mathrm{GeV}^2$ including uncertainties (shaded bands) compared to the CTEQ4M set (dashed curves).

At the starting scale, Q_o^2, the light valence quarks (u_v and d_v) and the sea of quark and anti-quarks (S) as well as the gluon (g) are attributed a given functional form. The measured structure functions are then described by the convolutions of the parton densities with the appropriate NLO matrix elements. In Fig. 1 the latest analysis of the BCDMS, CCFR, E665, H1, NMC, SLAC and ZEUS DIS measurements by Botje [1] gives the parton densities and their associated uncertainties. The uncertainties are determined from a full treatment of the systematic uncertainties of the data, varying the strong coupling constant ($\Delta\alpha_S(M_Z) = \pm 0.005$), varying the renormalisation and factorisation scale uncertainty from $Q^2/2$ to $2Q^2$, and assessing effects due to uncertainties on the strange sea, nuclear effects and the charm threshold (treated here as a light quark above threshold). The analysis is noteworthy in that care has been taken to provide the correlation coefficients for each of the parton densities. The fit agress with the latest CTEQ and MRST fits, within the uncertainties of up to 10% on each parton density at $Q^2 = 10\ \mathrm{GeV}^2$.

HERA Structure Function Measurements

HERA $F_2(x, Q^2)$ measurements extend to: low y ($y_{\mathrm{HERA}} \sim 0.005$) providing overlap with the fixed-target experiments; very low x ($x \lesssim 10^{-5}$) at low Q^2 exploring the transition region from soft to hard physics; high y ($y \to 0.8$) giving sensitivity to F_L; high $x \to 0.7$ probing sensitivity to electroweak effects in F_2 and xF_3 as well as constraining the valence quarks at large Q^2.

In Fig. 2 recent ZEUS F_2 data, as well as fixed target data from E665 and NMC, are plotted as function of Q^2 for fixed values of x. The observed scaling violations are intimately coupled with the rise of F_2 with decreasing x via the gluon density (in leading order $dF_2/d\ln Q^2 \sim xg(x)$ neglecting sea quark contributions). In order to study these scaling violations, a compact parameterisation $F_2(x) = A(x) + B(x)\log_{10} Q^2 + C(x)(\log_{10} Q^2)^2$ has been fitted, indi-

cated by the full line. The F_2 points are observed to rise significantly at low x with a tendency to flatten at the lowest x values. Lines of fixed centre-of-mass energy $W^2 = Q^2(1/x - 1)$ are indicated by the dashed lines. The derivative $dF_2/d\log_{10} Q^2 = B(x) + C(x)\log_{10} Q^2$ is plotted in Fig. 3 for constant W as a function of Q^2 (upper) and x (lower plot), motivated by similar theoretical plots in an analysis of low-x data by Golec-Biernat and Wüsthoff [2], incorporating saturation effects. The turnover of the derivative occurs at higher Q^2 (or x) for increasing W, consistent with predictions from various models which go beyond the DGLAP formalism. The DGLAP formalism itself is however also sufficiently flexible to describe the data, provided that the gluon (proportional to the derivative) decreases significantly at low (x, Q^2). The behaviour of the HERA low (x, Q^2) data remains a challenge to our understanding of QCD: this presentation of the data represents one way in which to address the problem, although there are various physical interpretations of the observed behaviour.

The contribution of F_L enters as a QCD correction to the total DIS cross-section. As such it provides a method to calibrate the gluon at low x. H1 [3] have used two methods to extract F_L from the reduced cross-section $\tilde{\sigma} = F_2 - y^2/Y_+ \cdot F_L$ at high y. This is the region where the scattered electron energy is low: in the H1 analysis scattered positrons are measured down to $E_{e'} \simeq 5$ GeV and backgrounds reduced by requiring the associated track to have correct charge. F_L is determined as a function of $Q^2 \geq 4$ GeV^2 by measuring local derivatives of $\partial\tilde{\sigma}/\partial \log y$ and observing deviations from a straight line (or a QCD fit for $Q^2 > 10$ GeV^2) at high y. The extracted F_L data are given in Fig. 4, compared to the H1 NLO QCD fit to H1, NMC and BCDMS F_2 data as well as to F_L data from SLAC and NMC. The data are in agreement with the QCD expectations although the precision is limited by statistics and uncertainties due to the input F_2.

Another method to calibrate the gluon distribution is to extract the contribution due to charm. $D^* \to (K\pi)\pi_s$ measurements in DIS provide a significant test of the gluon density of the proton determined from the scaling violations of F_2. They also help to constrain theoretical uncertainties in the fits to F_2 where different prescriptions for charm production are adopted. The D^* data are extrapolated outside the measured range of η, p_T to obtain the charm cross-section and hence $F_2^{c\bar{c}}$. The ratio $F_2^{c\bar{c}}/F_2$ is plotted in Fig. 5 as a function of x for four Q^2 values, compared to the NLO QCD expectations, where the dashed curves correspond to the uncertainty due to the parton distributions from the NLO fit. There is an overall normalisation uncertainty of approximately 10% (not shown) due (mainly) to the charm hadronisation fraction to D^*. At high W (or low x), the charm contribution to F_2 is significant (up to 30%) and therefore a careful treatment of charm production is required in any analysis of low (x, Q^2) data. The threshold region of of $x \simeq 10^{-2}$, where the charm cross-section is changing rapidly, is also important in consideration of the CCFR-NMC discrepancy.

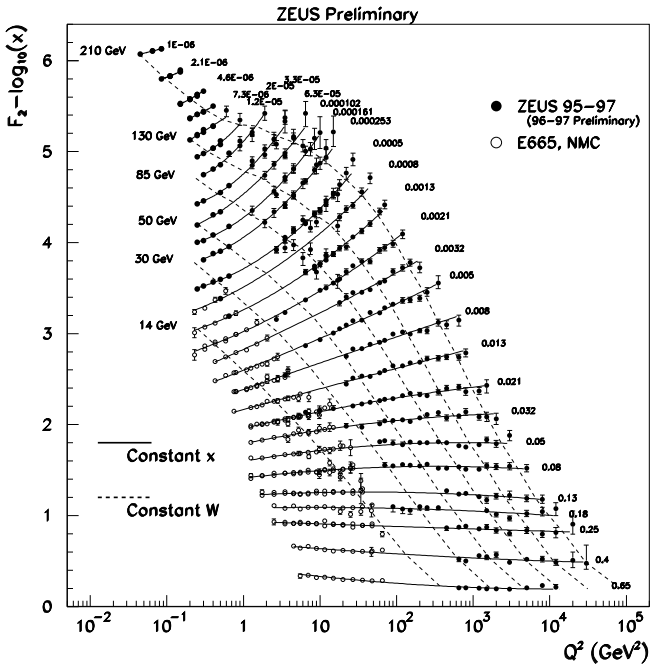

FIGURE 2. ZEUS, E665 and NMC $F_2 - \log_{10} x$ values versus Q^2. Fixed x values are indicated by the full lines and on the right hand side of the plot. Fixed W values are indicated by the dashed lines and on the left hand side of the plot.

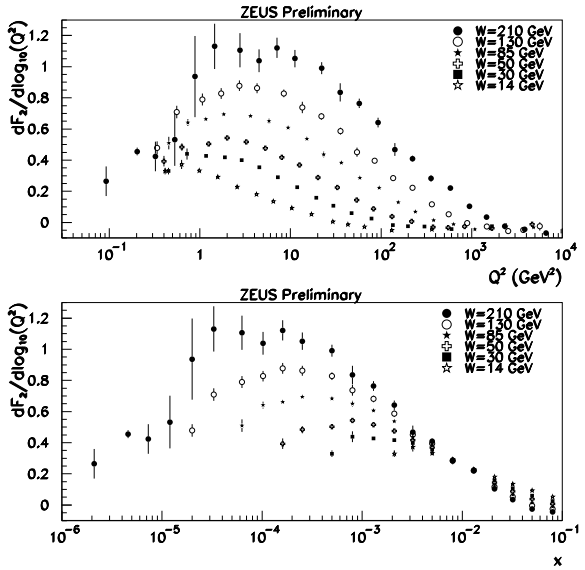

FIGURE 3. Derivatives of F_2 with respect to $\log_{10} Q^2$ for fixed W values indicated by the symbols. In the upper plot the data are plotted as a function of Q^2 and in the lower plot as a function of x.

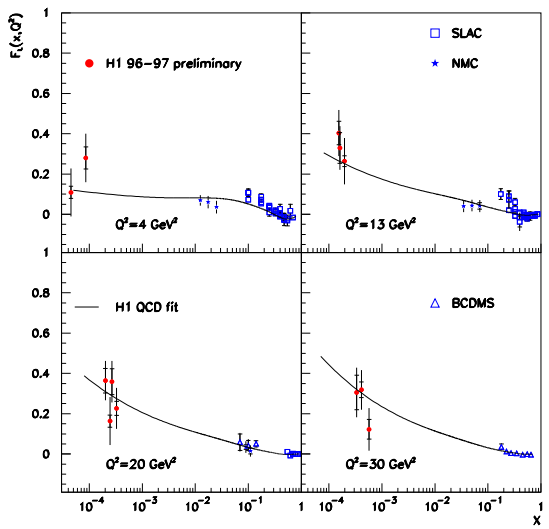

FIGURE 4. H1 determination of F_L versus x for four values of Q^2, compared to the NLO QCD fit expectation and data from BCDMS, NMC and SLAC.

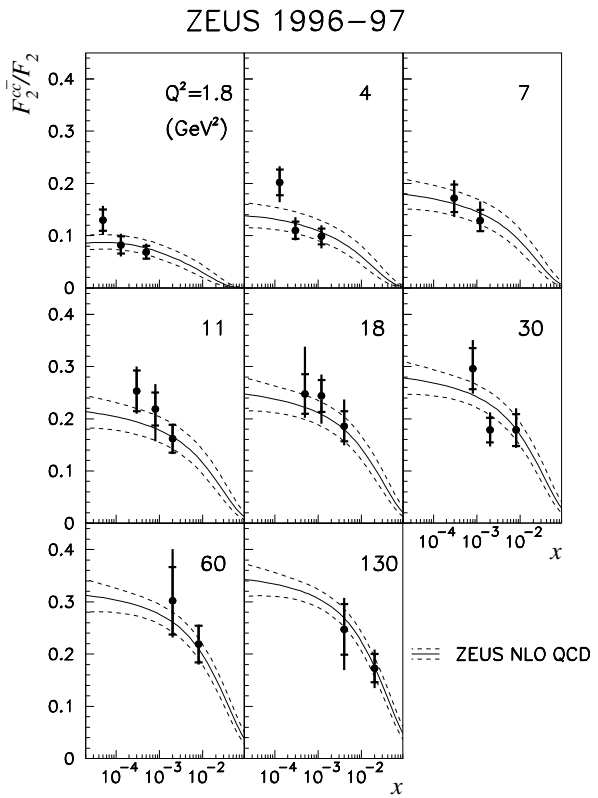

FIGURE 5. ZEUS ratio of $F_2^{c\bar{c}}/F_2$ as a function of x for four values of Q^2, compared to NLO QCD expectations.

Comparison of νN and lN Data

To leading order the muon (NMC) and neutrino (CCFR) structure functions are related by the "5/18ths rule" from quark counting. Here the strange sea enters as a correction, since $s \to c$ production is reduced in νN scattering due to the charm mass. The original CCFR analysis, where data were corrected using the dimuon result to constrain the strange sea, lay significantly ($\simeq 20\%$) above the NMC data for all values of Q^2 at $x < 0.1$. Advances in the H1 and ZEUS analyses of low y data, lead to a region of overlap where the HERA and fixed-target experiments can be compared with a precision of $\simeq$ 5%. In Fig. 6, a comparison of the CCFR (νN), H1, NMC and E665 (lN) data indicates that the discrepancy lies with the treatment of the CCFR data which is significantly above the lN data at low x.

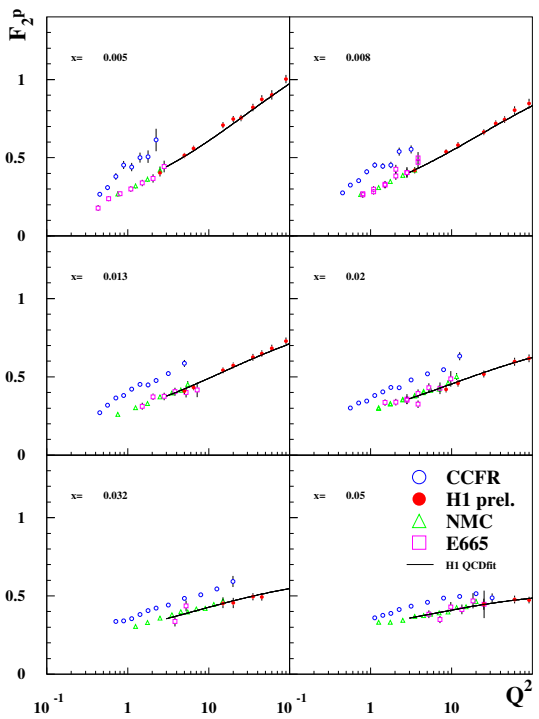

FIGURE 6. Original CCFR analysis compared to H1, E665 and NMC F_2 data. The F_2 data are plotted as a function of Q^2 for various x values. The full line is the H1 NLO QCD fit.

The HERA comparisons were made in parallel with a re-analysis of CCFR data by Yang and Bodek, reported at this conference [4]. The previous CCFR analysis used a slow rescaling variable $\xi = x(1 - m_c^2/Q^2)$, where m_c is the effective charm mass, in order to suppress charm production and correct F_2. In the latest CCFR analysis no explicit correction is made to the F_2 data for charm (or heavy target) effects. Various NLO treatments of charm are now available which allow data to be compared more precisely. The variable flavour scheme, adopted by CTEQ and MRST with different approaches to the threshold behaviour and fixed-order

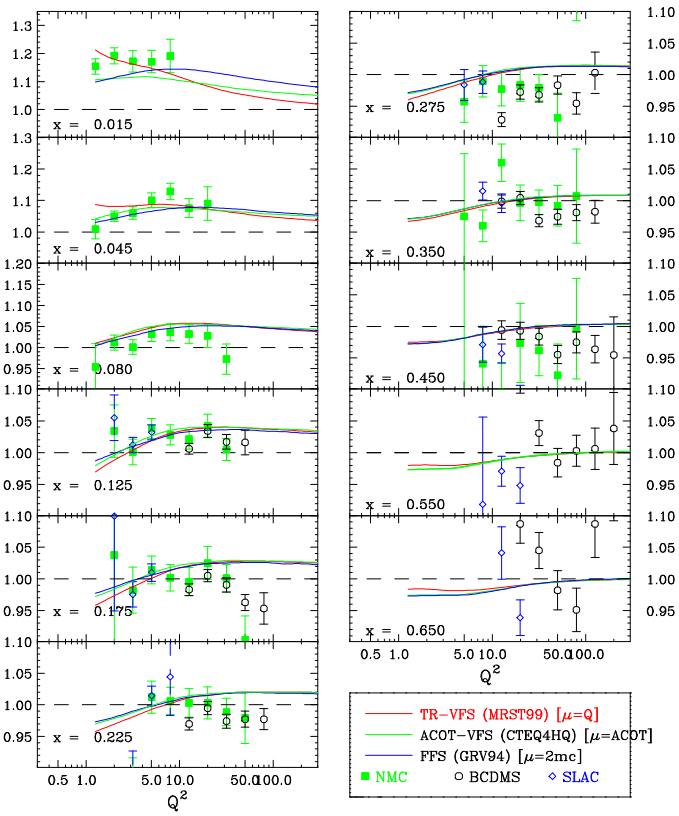

FIGURE 7. Model-independent CCFR analysis of the ratio of $5/18F_2^{\nu N}/F_2^{lN}$ as a function of Q^2 in various x intervals, compared to NLO calculations incorporating various treatments of charm. The CCFR data is divided by NMC, BCDMS and SLAC data.

treatment, handle charm as another parton in the proton, a good approximation for $Q \gtrsim m_c$. The fixed flavour scheme (FFS), adopted by GRV, treats charm as generated dynamically in NLO QCD, a good approximation for $Q \simeq m_c$. The ratio of $5/18F_2^{\nu N}/F_2^{lN}$ is plotted in Fig. 7. A clear departure from unity is observed at the lowest x values. The data are compared to NLO charm calculations from MRST, CTEQ and GRV which differ somewhat in shape, but provide a good description of the data ratios at all values of x. The difference in xF_3 from ν and $\bar{\nu}$ data ($\Delta xF_3^{\nu-\bar{\nu}}$, not shown) is also sensitive to charm production and provides an additional constraint on the calculations.

The significant discrepancy between $F_2^{\nu N}$ and F_2^{lN} data is thus resolved. The area is now open for more detailed comparisons of NLO charm methods, constraints on the strange sea from the ratio of CCFR to NMC and HERA data compared to CCFR dimuon data as well as an understanding nuclear shadowing corrections for νFe (CCFR) data. In addition new data from NuTeV tagging ν and $\bar{\nu}$ beams will provide more information on $\Delta xF_3^{\nu-\bar{\nu}}$, as well as improving the measurement of $\sin^2\theta_W$.

Inclusive Jet Production at the Tevatron

The Tevatron collider provides a unique opportunity to study the properties of hard interactions in $p\bar{p}$ collisions at short distances. CDF and DØ have measured jet cross-sections at $\sqrt{s} = 1800$ GeV over ten orders of magnitude in $d^2\sigma/dE_T d\eta$ up to $E_T = 500$ GeV, half-way to the kinematic limit. These data indicate that the gluon should be enhanced at large x compared to direct photon measurements. One open area for further experimental and theoretical investigation is in this measurement at different energies. The ratio of the inclusive jet cross-section at $\sqrt{s} = 630$ GeV over $\sqrt{s} = 1800$ GeV is plotted in Fig. 8 as a function of scaled jet transverse energy $x_T = 2E_T/\sqrt{s}$. The ratio should lead to a partial cancellation of experimental and theoretical systematics [5]. However, it is clear that there is an experimental discrepancy at the lowest values of $x_T \lesssim 0.15$. In addition, the data lie below the NLO QCD predictions at all values of x_T. Two explanations have been proposed: first that different renormalisation scales could be used for the theoretical calculations at the two energies; second that a relatively small shift in jet energies by approximately 3 GeV (due to non-perturbative jet pedestal or underlying event effects) brings the theory in agreement. The forthcoming Run II will provide higher energy data in order to clarify these issues.

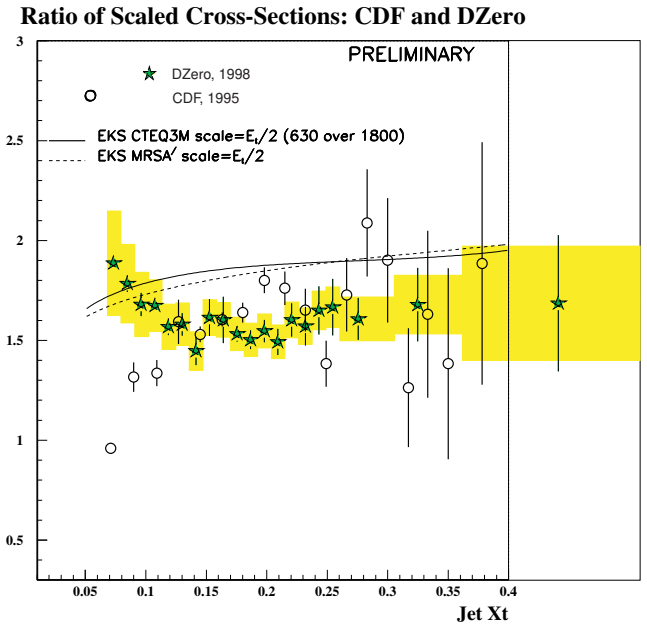

FIGURE 8. Ratio of CDF and DØ inclusive jet cross sections at $\sqrt{s} = 1800\ GeV$ to $\sqrt{s} = 630\ GeV$, as a function of $x_T = 2E_T/\sqrt{s}$, compared to NLO QCD. The shaded band indicates the DØ energy scale uncertainty

High Q^2 Cross-Sections at HERA

The HERA collider provides a unique window to explore ep interactions at the highest energies, extending the range of momentum transfer Q^2 by about two orders of magnitude compared to fixed-target experiments. As the HERA luminosity increases we explore the region of $Q^2 \sim 10^4$ GeV^2, where electroweak effects play a rôle. It is in this unexplored kinematic region that we are sensitive to deviations from the standard model (SM). The theoretical uncertainties on the SM $e^{\pm}p$ NC and CC cross-sections were determined as discussed with respect to the parton densities of Fig. 1 and correspond to $\simeq$ 6-8% on the NC cross-sections and $\simeq$ 6-12% on the CC cross-sections at the highest accessible Q^2 values. The measured cross-sections generally agree with theory within these uncertainties and therefore represent a benchmark for the standard model. The example cross-sections, discussed below, are corrected to the electroweak Born level.

The e^+p charged-current cross-section [7,8] is sensitive to the valence d-quark distribution in the proton

$$\frac{d^2\sigma_{e^+p}}{dx\,dQ^2} \simeq \frac{G_F^2}{2\pi}\left(\frac{M_W^2}{Q^2+M_W^2}\right)^2 [\overline{u}+\overline{c}+(1-y)^2(d+s)].$$

In the upper plot of Fig. 9 the ZEUS cross-section is described by the SM, falling over four orders of magnitude. The ratio of the data to the SM, adopting the CTEQ4D PDF, is shown in the lower plot of Fig. 9 where good agreement is observed as a function of x for $Q^2 > 400$ GeV^2. Comparison of the data with the PDF uncertainties (shaded band) indicates that the data will help to constrain the d-quark densities at large x. The uncertainties on the data are large in this region, but an increase of the ratio of d/u quarks, such as that proposed by Yang and Bodek [6] results in better agreement with the data than the standard PDFs. The CC cross-section is suppressed relative to NC exchange due to the W propagator term: this characteristic dependence on Q^2 has been fitted to yield values for the mass of the exchanged space-like W-boson. The 'propagator-mass' fit value (with G_F fixed) of

$$M_W = 81.4^{+2.7}_{-2.6}(\text{stat.})\pm 2.0(\text{sys.})^{+3.3}_{-3.0}(\text{PDF})\ \text{GeV}$$

agrees with the PDG value of $M_W = 80.41 \pm 0.10$ GeV obtained from time-like production of W bosons at LEP and the Tevatron. The consistency of the data with the SM has been checked using the PDG values for G_F, α, M_Z and M_t, yielding a consistent value of

$$M_W = 80.50^{+0.24}_{-0.25}(\text{stat.})^{+0.13}_{-0.16}(\text{sys.})\pm 0.31(\text{PDF})^{+0.03}_{-0.06}(\Delta M_t, \Delta M_H, \Delta M_Z)\ \text{GeV}.$$

This result is in agreement with the value of $M_W = 80.35 \pm 0.21$ GeV obtained by NuTeV [9].

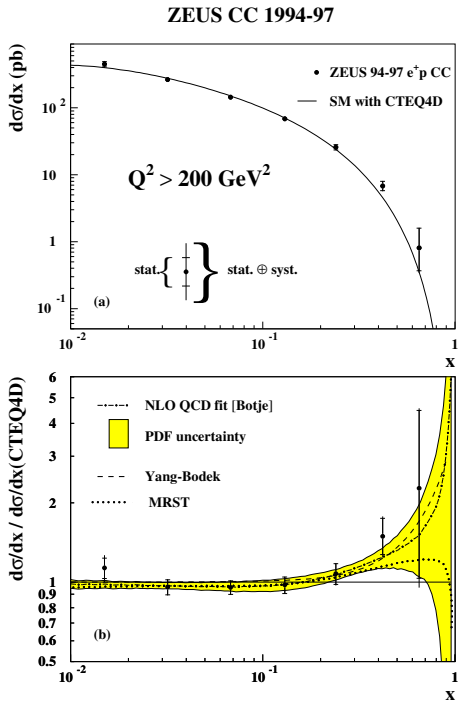

FIGURE 9. ZEUS charged current cross-section $d\sigma^{CC}(e^+p)/dx$ versus x for $Q^2 > 400$ GeV^2 and ratio with respect to the standard model prediction using the CTEQ4D PDF (lower plot). The curves and shaded band in the lower plot correspond to the NLO PDF fits described in the text.

The NC cross-sections are particularly sensitive to the valence u-quark distribution in the proton

$$\frac{d^2\sigma_{e^\pm p}}{dx\,dQ^2} \simeq \frac{2\pi\alpha^2}{xQ^4}[Y_+F_2(x,Q^2) \mp Y_-xF_3(x,Q^2)].$$

Here, F_2 is the generalised structure function, incorporating γ and Z terms, which is sensitive to the singlet sum of the quark distributions $(xq + x\overline{q})$ and xF_3 is the parity-violating (Z-contribution) term which is sensitive to the non-singlet valence quark distributions $(xq - x\overline{q})$. The $e^\pm p$ data are now becoming sensitive to the difference in sign of the xF_3 contribution (due mainly to electroweak γZ interference effects) which suppresses (enhances) the e^+p (e^-p) NC cross-section by $\sim 30\%$ for $Q^2 > 10,000$ GeV^2. This is illustrated in Fig. 10 where the H1 reduced cross-section for e^+p (820 GeV) and e^-p (920 GeV) data is compared. A further step has been taken in the ZEUS analysis where the difference of the cross-sections (modified slightly due to the different beam energies) yields a first measurement of xF_3 [10]. In Fig. 11 the scaling of xF_3 is shown as a function of Q^2 compared to the CTEQ4D and MRST(99) PDFs: the statistical precision is currently limited, although the systematic precision on data and theory is good, boding well for a future determination of $\alpha_S(M_Z)$.

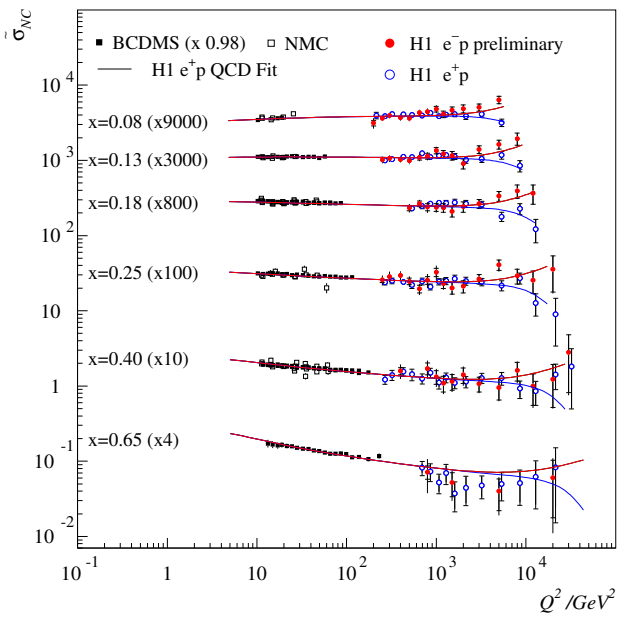

FIGURE 10. H1 neutral current reduced cross-section as a function of Q^2 for various values of x. The e^+p and e^-p data are compared to the NLO QCD fit expectations (full line) obtained from fitting the e^+p data.

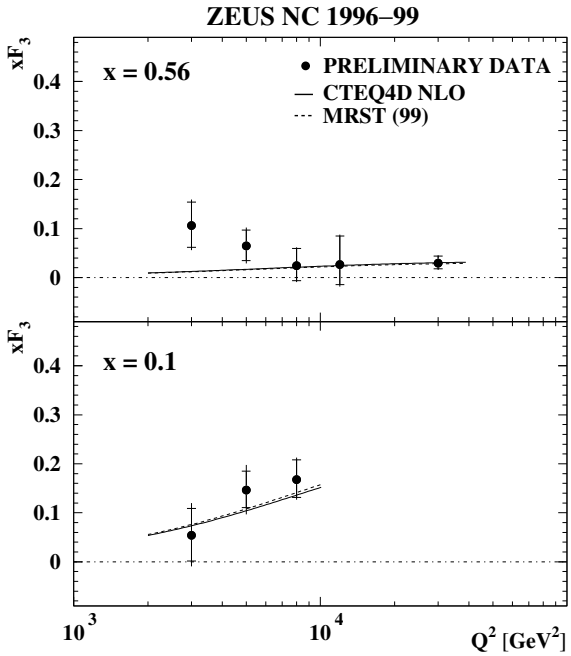

FIGURE 11. ZEUS xF_3 data extracted from the difference of the e^-p and e^+p neutral current cross-sections, compared to the CTEQ4D and MRST(99) PDF expectations.

Outlook: The first phase of HERA running from 1992-2000 is now complete. An upgrade of HERA during 2000-2001 will enable luminosities to be increased by a factor of 4-5. In the longer term, DESY has recognised a future programme for ep physics by ensuring that the proposed TESLA 500 GeV e linear collider is capable of combining with the HERA proton ring to provide the next generation of deep inelastic scattering measurements. The historical perspective of such an endeavour is illustrated in Fig. 12, where the resolved dimension (d [fm] $= 0.2/Q_{\max}$ [GeV]) is plotted as a function of year. Progress on the path of DIScovery started with Rutherford, observed to be 30 years ahead of his time, and is planned to reach down to sub-attometre distances with the TERA collider.

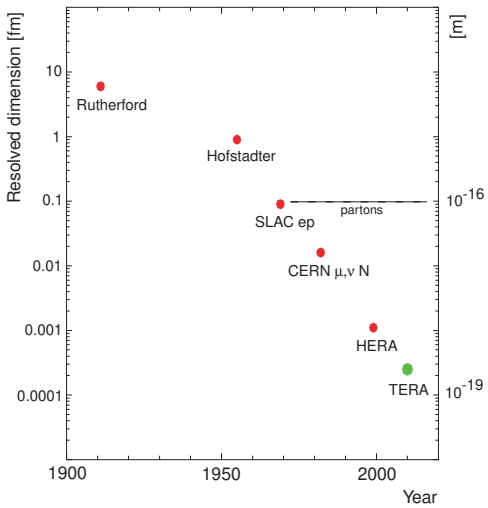

FIGURE 12. Resolved dimension as a function of year including the proposed TERA (=TESLA⊗HERA) collider.

Acknowledgements: It is a pleasure to thank the organisers for an excellent conference. Many thanks to Ian Bertram, Chris Cormack, Doris Eckstein, Brian Foster, Sergey Levonian, Jason Webb, Un-Ki Yang, Rik Yoshida and all the speakers in the structure functions parallel session for their help and advice.

REFERENCES

1. M. Botje, Eur. Phys. J. C14 (2000) 285.
2. K. Golec-Biernat and M. Wüsthoff, Phys. Rev. D59 (1999) 014017.
3. S. Levonian, CIPANP2000 proceedings.
4. U.K. Yang, CIPANP2000 proceedings.
5. R. Hirosky, CIPANP2000 proceedings.
6. U.K. Yang and A. Bodek, Phys. Rev. Lett. 82 (1999) 2467.
7. H1 Collab., C. Adloff et al., Eur. Phys. J. C13 (2000) 609.
8. ZEUS Collab., J. Breitweg et al., Eur. Phys. J. C12 (2000) 411.
9. CCFR/NuTeV Collab., K.S. McFarland et al., Eur. Phys. J. C1 (1998) 509.
10. C. Cormack, CIPANP2000 proceedings.